



Spontaneously super-hygroscopic MOF-gel microreactors for efficient detoxification of nerve agent simulant in atmospheric environments

Xuejiao Wang^{a,b}, Jing Yang^c, Ming Zhang^a, Qian Hu^b, Bai-Xue Li^a, Jin Qu^a, Zhong-Zhen Yu^{b,*}, Dongzhi Yang^{a,*}

^a State Key Laboratory of Organic-Inorganic Composites, College of Materials Science and Engineering, Beijing University of Chemical Technology, Beijing 100029, China

^b Beijing Key Laboratory of Advanced Functional Polymer Composites, Beijing University of Chemical Technology, Beijing 100029, China

^c College of Chemistry and Chemical Engineering, Hunan Normal University, Changsha 410081, China

ARTICLE INFO

Keywords:

Hygroscopicity
Nerve agents and simulants
Catalytic hydrolysis
Poly(N-isopropylacrylamide) gel
Metal-organic frameworks

ABSTRACT

We design a spontaneously super-hygroscopic alkaline microreactor by photoinduced integration of Zr-MOF catalyst and alkaline poly(dimethylaminoethyl acrylate) onto LiCl-salinized poly(N-isopropylacrylamide) gel, generating a microenvironment with non-volatile polymeric base and non-bulk water for detoxification of a typical nerve agent simulant, dimethyl 4-nitrophenyl phosphate (DMNP), in atmospheric environments. The super-hygroscopic gel with directional microchannels facilitates the absorption, transport and storage of water under different humidities, and exhibits fast hygroscopic efficiency with a high moisture absorption capacity of 6.4 g g^{-1} . The integrated microreactor achieves simultaneous water uptake and catalytic hydrolysis of DMNP in an atmospheric environment with an initial half-life of $\sim 1.9 \text{ h}$ and a final conversion of 95.5%, which is attributed to the synergistic catalytic microenvironment of the exposed Zr-MOF catalyst, the polymeric base, and the water from moist air. This work provides a feasible strategy for designing spontaneously hygroscopic microreactors for detoxifying nerve agent simulants in atmospheric environments.

1. Introduction

The detoxification of chemical warfare agents (CWAs) is a necessary and urgent task of human society because of their irreversible destructive effect on nervous systems and the lethal erosion of skins [1,2]. Currently, most protection systems are based on activated carbon filters that can capture gases, aerosols or liquids, but they often suffer from their low responsiveness, limited adsorption capacity, and attenuating efficacy, as well as the risk of potential secondary hazards [3–6]. Metal-organic frameworks (MOFs) are promising catalysts for the detoxification of CWA simulants because of their diverse porous structures, tunable pore sizes, and functionalized linkers [7–13]. In particular, Zr-MOFs (e.g., UiO-66, NU-1000, and MOF-808) with exposed bimetallic Zr-OH-Zr active sites can efficiently catalyze the hydrolysis of organophosphate bond-containing nerve agents and simulants in aqueous alkaline solution [14–16].

The catalytic hydrolysis of the typical nerve agent simulant dimethyl 4-nitrophenyl phosphate (DMNP) by Zr-MOF is highly dependent on aqueous alkaline solutions. The lack of water hinders the catalytic

hydrolysis of DMNP in practical atmospheric environments. The N-ethylmorpholine (NEM) buffer is a widely used nucleophile for promoting the cleavage of organophosphate bonds and neutralizing acidic products in liquid-phase [17,18]. For example, the conversion of DMNP catalyzed by UiO-66-NH₂ could be over 90% in the NEM buffer and the catalytic activity is 20-fold higher than that of UiO-66, because the proximal amine group of the UiO-66-NH₂ can act as a Brønsted base [19]. In the absence of the NEM buffer, the UiO-66-NH₂ exhibits a sharply reduced catalytic efficiency [20,21]. Due to the drawbacks of the NEM in terms of toxicity and volatility, non-volatile bases are developed as alternatives such as amine-modified Zr-MOFs [22] and amine-based polymers of polyethyleneimine (PEI) [23] and poly-amidoamine (PAMAM) [24,25] for the applications of protective masks. For example, Chen et al. [26] and Mian et al. [27] demonstrated that the hydrolysis rates of the DMNP catalyzed by Zr-MOF (NU-1600) in linear PEI buffer (2.9 min) and Zn-MOF (MFU-4l) in PAMAM buffer ($\sim 1 \text{ min}$) were comparable to those in the NEM buffer. Although the amine-based polymers are feasible in catalyzing the hydrolysis of DMNP in liquid-phase, their efficacy in the absence of bulk water has rarely been

* Corresponding authors.

E-mail addresses: yuzz@mail.buct.edu.cn (Z.-Z. Yu), yangdz@mail.buct.edu.cn (D. Yang).

<https://doi.org/10.1016/j.apcatb.2023.122516>

Received 21 November 2022; Received in revised form 1 February 2023; Accepted 22 February 2023

Available online 23 February 2023

0926-3373/© 2023 Elsevier B.V. All rights reserved.

explored.

For a wearable protective device, the detoxification of nerve agents and simulants in atmospheric environments is necessary for its practical application with the advantages of selective capture, rapid response, and on-demand protection. Farha et al. [28] catalytically hydrolyzed DMNP with a PEI/MOF-808/fiber composite at a relative humidity (RH) of 50% and exhibited an initial half-life ($t_{1/2}$) of 1.6 h, demonstrating that the catalytic hydrolysis could be achieved by using the moisture from the air. Recently, Baek et al. [29] reported the catalytic hydrolysis of DMNP with a PMMA/PEI/Uio-66 composite film at the RH of 99% with a half-life of 4.8 h. The moisture absorption capacity of MOF powders is strongly affected by their pore size, porosity, and the limited water storage space within the framework. On the basis of the water adsorption isotherms, specific relative humidity and pressure are required to achieve the saturated water contents of MOFs of Uio-66 (0.44 g g^{-1}), Uio-66-NH₂ (0.39 g g^{-1}), and MOF-808 (0.6 g g^{-1}) at 40% RH, and NU-1000 (1.4 g g^{-1}) at 70% RH at 298 K [30], which would limit the application of MOFs in a wider relative humidity range. Polymer-based atmospheric water collectors with hygroscopic inorganic salts have been served as air dehumidification, heal-pumps and chillers, and indoor humidity control due to their excellent moisture absorption capacity, rapid hydration rate, long-lasting water retention, wide applicability and high designability [31–34]. To the best of our knowledge, the collection of atmospheric water for detoxification of nerve agent simulants in simulated practical environments is promising but has not been reported yet.

Herein, for efficient detoxification of nerve agent simulant in atmospheric environments, a spontaneously super-hygroscopic alkaline microreactor is designed by spray-coating and copolymerization of alkaline dimethylaminoethyl acrylate (DMAEA) with synthesized Uio-66-acrylamide (Uio-66-AM) nanoparticles onto the three-dimensional (3D) LiCl-salinized poly(N-isopropylacrylamide) (PNIPAM) gel substrate with a plain-and-basin structure. The resultant MOF@PDMAEA@LiCl@PNIPAM gel (MG) microreactor consists of the MOF catalyst with exposed catalytic active sites, the polymerized DMAEA (PDMAEA) as a non-volatile base, and the spontaneously super-hygroscopic LiCl@PNIPAM gel with open directional microchannels for fast mass transport. The MG microreactor exhibits fast water uptake, high moisture absorption capacity of up to 6.4 g g^{-1} , and satisfactory catalytic hydrolysis of DMNP over a wide range of relative humidity because of the integrated synergistic catalytic microenvironment under atmospheric conditions. Moreover, two different detoxification mechanisms of DMNP in liquid and solid phases are investigated in detail. Catalyzed by MOF powders in liquid-phase, the cleavage of DMNP is driven by nucleophilic substitution of -OH groups generated by the alkaline buffer. By contrast, the DMNP is hydrolyzed by the non-bulk water provided by the MG microreactor under atmospheric conditions, and the resulting acidic product is dissociated by the proximal polymeric base via proton transfer to further promote the reaction.

2. Experimental section

2.1. Materials

Zirconium chloride (ZrCl_4), N-isopropylacrylamide (NIPAM), acrylic anhydride, 2-aminoterephthalic acid ($\text{H}_2\text{N-H}_2\text{BDC}$, 98%), dimethylaminoethyl acrylate (DMAEA), N,N-methylenebisacrylamide (MBA), and N-ethylmorpholine (NEM) were purchased from Aladdin (China). Lithium chloride (LiCl), and 2-hydroxy-2-methylpropiophenone (HMPP) were bought from Sigma-Aldrich. Dimethyl formamide (DMF), dichloromethane (CH_2Cl_2), dimethyl sulfoxide (DMSO), hydrochloric acid (HCl), deuterated DMSO ($\text{DMSO-}d_6$), and ethanol were obtained from Beijing Chemical Reagents (China). Dimethyl 4-nitrophenyl phosphate (DMNP) was supplied by Alta Scientific (China). All the chemicals and reagents were used as received without further purification.

2.2. Syntheses of Uio-66-NH₂ and Uio-66-AM

Zirconium chloride (57 mg, 0.245 mmol), and 2-aminoterephthalic acid (44 mg, 0.245 mmol) were dissolved in the mixture of 15 mL DMF and 1 mL HCl. The resultant solution was put in a Teflon-lined autoclave for reactions at 120 °C for 12 h. After cooling to the ambient temperature, the product (Uio-66-NH₂) was collected by centrifuging at 6000 rpm for 5 min, and washed with DMF and ethanol for three times sequentially, suction-filtrated, vacuum-dried at 80 °C, and activated by heating at 120 °C for 3 h. Furthermore, the as-synthesized Uio-66-NH₂ (60 mg, 0.2 mmol) was mixed with acrylic anhydride (126 mg, 1 mmol) in 1 mL CH_2Cl_2 in a vial. The vial was then sealed for reactions at 25 °C for 4 days, and the resultant product (Uio-66-AM) was rinsed with CH_2Cl_2 and ethanol in sequence for several times, and vacuum-dried at 80 °C for 12 h.

2.3. Synthesis of patterned PNIPAM hydrogels

A pre-gel solution was prepared by dissolving 0.5 g of NIPAM monomer, 25 mg of MBA crosslinker, and 10 mg of HMPP photoinitiator in 5 mL of deionized water under magnetic stirring for 30 min. After purging with nitrogen gas for 10 min, the solution was injected into a mold that was equipped with photomasks with circular patterns of 300, 500 and 1000 μm diameters on the silicone pad between two glass slides, and photopolymerized under a Xenon lamp with a light intensity of 1 W cm^{-2} for 5 min. The resulting patterned PNIPAM hydrogels (PHs) were taken out of the mold and immersed in deionized water to remove excess ingredients.

2.4. Cold-hot cyclic treatment and salinization

To rearrange the polymer chains via intermolecular hydrogen bonding, the PNIPAM hydrogel was immersed sequentially in cold (5 °C) and hot deionized water (60 °C) for 15 min per cycle, and the cold-hot cyclic treatment was repeated for three times. Subsequently, the sample was quickly immersed in an aqueous solution of LiCl (50 mg mL^{-1}) at 5 °C for 12 h for the interaction of the salt ions with the polymer chains. The resultant LiCl@PNIPAM hydrogel was designated as LH.

2.5. Synthesis of MOF@PDMAEA@LiCl@PNIPAM hydrogels

60 mg of Uio-66-AM was mixed well with 4 mL of DMAEA monomer (with 1 wt% HMPP), and the mixture was then dispersed in ethanol to generate diluents with the MOF contents of 1, 2 and 3 mg mL^{-1} . The diluents were sprayed on the patterned surfaces of the LH using a spray gun with a 0.5 mm aperture under 2 bar air pressure, and simultaneously irradiated with a Xenon lamp of 1 W cm^{-2} for 5 min to copolymerize the DMAEA monomer with the acrylamide moiety of the Uio-66-AM. The resultant MOF@PDMAEA@LiCl@PNIPAM hydrogel (MH) was immersed in deionized water to remove excess ingredients.

2.6. Unidirectional-freezing and freezing-drying of the hydrogels and their moisture absorption capacities

The synthesized hydrogels were unidirectionally frozen by placing on copper disks that were partially immersed in liquid nitrogen, and freeze-dried to obtain PNIPAM gel (PG), LiCl@PNIPAM gel (LG), and MOF@PDMAEA@LiCl@PNIPAM gel (MG) with the thickness of $\sim 1 \text{ mm}$. The MG samples with different MOF loadings were designated as MG-1, MG-2, and MG-3, and the MG samples with different basin sizes were designated as MG-300, MG-500 and MG-1000. For comparison, the random LiCl@PNIPAM gel (RG) with a patterned surface and conventional LiCl@PNIPAM gel (CG) without a patterned surface were prepared by random freezing at -20 °C followed by freeze-drying. To evaluate the water uptake properties, the gels were placed in a JYH-66 temperature and humidity chamber at 25 °C and different RHs of 90%,

60% and 30%. The gels were weighed periodically on a precision balance and the average value of five repeated tests was taken to assess their moisture absorption capacity.

2.7. Characterization

The gels and MOF powders were observed with a Hitachi S-4700 scanning electron microscope (SEM) equipped with an energy-dispersive spectroscopy (EDS) device, a Hitachi H-7700 transmission electron microscope (TEM), a Bruker multimode 8 atomic force microscope (AFM) under a tapping mode in air, and a Leica TCS SP8 DLS confocal laser scanning microscope (CLSM) with a 10x objective lens after dyeing with 0.01 mg mL⁻¹ Rhodamine B solution. The chemical compositions and structures were characterized using a D8 Advance X-ray diffractometer (XRD) with a CuK α radiation, a Nicolet Nexus 670 Fourier-transform infrared (FTIR) spectrometer, a RSCAKAB 250X X-ray photoelectron spectroscopy (XPS), an iCAPQc inductively coupled plasma optical emission spectrometer (ICP-OES), a TA Q50 thermogravimetric analyzer (TGA) at a heating rate of 10 °C min⁻¹, and an inVia Reflex micro-Raman spectrometer with a laser wavelength of 785 nm. Specific surface areas and pore sizes of the MOFs were measured by a Micromeritics ASAP 2460 Brunauer-Emmett-Teller (BET) surface area measurement on the basis of N₂ adsorption and desorption analysis. The absorbance spectra were collected with a Shimadzu UV-3600 UV-visible (UV-vis) spectrophotometer (300–500 nm). ¹H and ³¹P nuclear magnetic resonance (NMR) spectra were recorded on an AV600 Bruker NMR spectrometer at the frequency of 600 MHz. Mass spectrometry (MS) analysis was performed using a Waters high-resolution mass spectrometer with a direct MS detector in positive and negative ion mode.

2.8. Hydrolysis of DMNP in liquid-phase

3 μ mol MOF catalyst (12 mol%, UiO-66-NH₂ or UiO-66-AM) was added to 1 mL alkaline buffer (0.45 M, NEM or DMAEA) in a 2 mL Eppendorf tube under vigorous stirring for 30 min. After 25 μ mol DMNP was added to the above suspension, 20 μ L aliquots were retrieved from

the reaction mixture at fixed intervals and diluted with 10 mL NEM aqueous solution (0.15 M). The ultraviolet absorption peak at 402 nm for the hydrolysis product p-nitrophenoxide (4-NP) was periodically monitored by the UV-vis spectra.

2.9. Hydrolysis of DMNP under atmospheric conditions

The catalytic hydrolysis of the DMNP under atmospheric conditions was carried out in the constant temperature and humidity chamber at 25 °C and at 90%, 60% and 30% RH. 12.5 μ mol DMNP was dropped on the surface of the MG samples with different MOF loadings (12, 6 and 3 mol%) in a glass Petri dish, and immediately transferred into the chamber. Samples were taken out at the scheduled time and digested in DMSO-*d*₆. The filtered supernatant was injected into a nuclear magnetic tube, in which the contents of organophosphorus compounds were quantitatively detected by ³¹P NMR measurements. For comparison, LG, UiO-66-AM, DMAEA, LG/UiO-66-AM (LG/MOF), LG/DMAEA, and UiO-66-AM/DMAEA (MOF/DMAEA) were used to catalyze the DMNP hydrolysis at 25 °C and 90% RH over 48 h. And the samples were subjected to the same digestion process, and the contents of organophosphorus compounds were quantified on the basis of the ³¹P NMR measurements.

3. Results and discussion

3.1. Construction of tunable 3D patterned PNIPAM gels

A scalable spontaneously super-hygroscopic alkaline microreactor is fabricated by synthesis of patterned PNIPAM hydrogel (PH), salinization with LiCl, coating with MOF nanoparticles and a polymeric base, unidirectional-freezing and freeze-drying (Fig. 1). Firstly, with the help of the photomask technology combined with polymerization-induced diffusion process, the 3D patterned PH is synthesized within 5 min under a simulated solar light intensity of 1 W cm⁻². After the cold-hot cyclic treatment by sequentially immersing the hydrogel in cold (5 °C) and hot deionized water (60 °C) to rearrange the polymer chains via intermolecular hydrogen bonding, the hydrogel is salinized in an

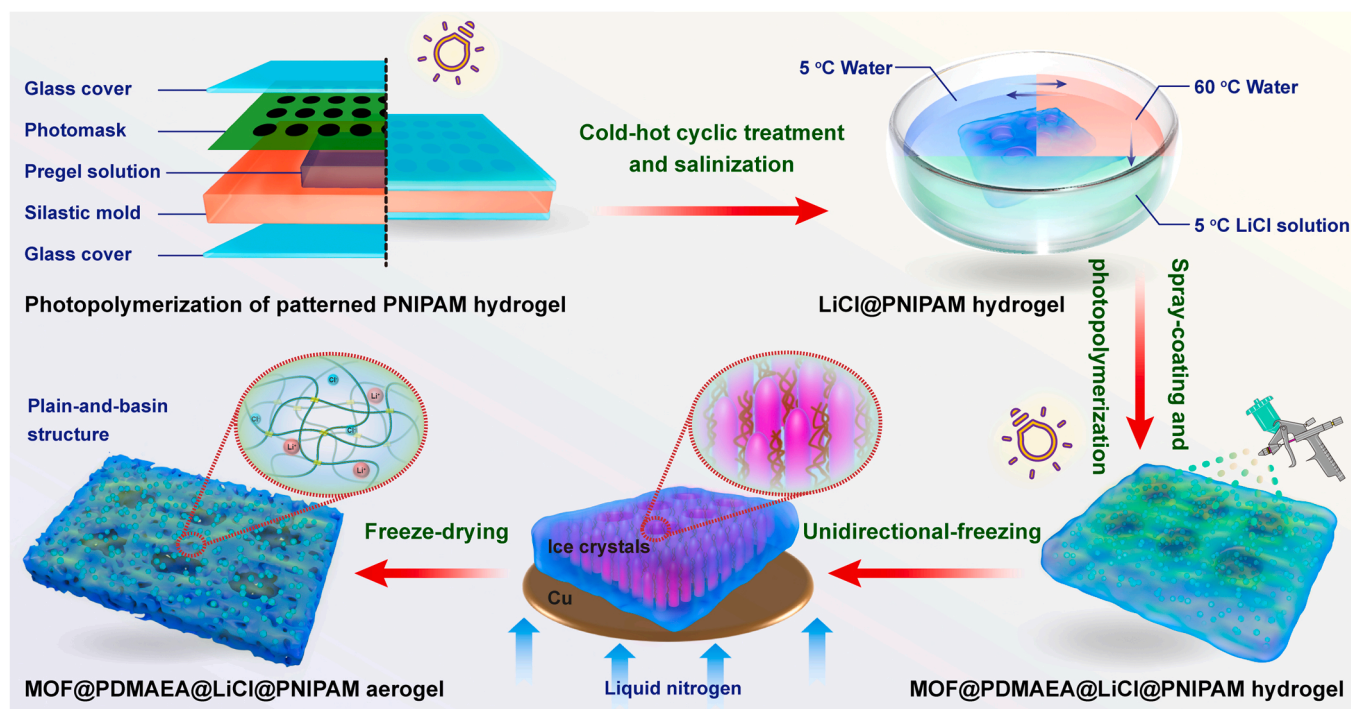


Fig. 1. Schematic illustrating the preparation of spontaneously super-hygroscopic MOF@PDMAEA@LiCl@PNIPAM gel by photopolymerization of PNIPAM, cold-hot cyclic treatment, salinization with LiCl, coating with MOF catalyst and PDMAEA base, unidirectional-freezing, and freeze-drying.

aqueous solution of LiCl, during which the hygroscopic component is anchored on the polymer chains via the Hofmeister effect to obtain the LiCl-salinized PNIPAM hydrogel (LH). Subsequently, the integration of MOF and amine-based polymer (PDMAEA) on the LH surface is achieved by spray-coating followed by photopolymerization of the DMAEA. Finally, the MOF@PDMAEA@LiCl@PNIPAM gel (MG) with directional microchannels for water transport and storage is generated by a liquid nitrogen-assisted unidirectional-freezing and subsequent freeze-drying. The hygroscopicity of LiCl, the water storage capacity of the patterned PNIPAM substrate, the catalytic activity of MOF nanoparticles, and the non-volatile PDMAEA base can endow the resultant MG microreactor with spontaneously super-hygroscopicity and high catalytic performances towards the detoxification of DMNP under atmospheric conditions.

The photopolymerization procedure of the patterned PNIPAM hydrogel is illustrated in Fig. 2. The simulated solar light goes through the photomask and exhibits a Gaussian intensity distribution with maximum intensity in the scope between the intersecting patterns, and its intensity decreases near the edges in view of light diffraction (Fig. 2a) [35,36]. After irradiating for ~ 1 min, the polymerization reaction is first initiated in the exposed regions, where the transparent monomer liquid changes to white hydrogel and gradually expands to the unexposed regions (Fig. 2b). It is seen that the monomers and radicals diffuse to the opposite directions in the local region driven by the chemical potential gradient of the reactants (Fig. 2c). The NIPAM monomers are rapidly consumed in the exposed regions and diffuse inward from surroundings (blue solid arrows), while the excessive radicals diffuse toward the periphery (orange dashed arrows).

The patterned surface of the hydrogel with a plain-and-basin structure is clearly recorded by a CLSM image (Fig. 2d), which is beneficial to the anchoring of the MOF nanoparticles and the PDMAEA as well as the attachment of water molecules in moist air. In the optical photographs of the patterned gels with different sizes under yellow light irradiation, the opaque regions are the plain parts, while the translucent bright regions are the basin parts (Fig. 2e-h). The corresponding SEM images (Fig. 2i-l) show that the basin sizes of the patterned PNIPAM gels (PG) range from

300 to 1000 μm . The larger basin size corresponds to deeper basin depth due to the relative diffusion of the monomers and radicals (Fig. S1). Note that over deep basins tend to cause the aggregation of MOF nanoparticles, which would adversely affect the exposure of the active sites of the MOF. The gels with basin sizes of ~ 500 μm are the optimal choice for anchoring and dispersing MOF nanoparticles.

3.2. Integration of LiCl-salinized PNIPAM gel with MOF and alkaline PDMAEA

To expose the MOF catalyst and ensure its synergistic catalysis with the non-volatile polymer base, the mixture of the UiO-66-AM with acrylamide groups and the unsaturated DMAEA monomers is spray-coated on the LH surface with a plain-and-basin structure followed by photopolymerization (Fig. 3a). Firstly, the acrylamide groups are grafted on the organic ligands of the parent UiO-66-NH₂ in CH₂Cl₂ solution of acrylic anhydride by the post-synthetic modification while maintaining the integrity of the MOF framework (Fig. 3b). The UiO-66-AM nanoparticles with an average size of ~ 80 nm (Fig. S2) are obtained by adjusting the amount of the modulator (HCl), the reaction temperature, and the reaction duration. The XRD pattern of the UiO-66-AM exhibits diffraction peaks at 7.3° , 8.4° and 25.6° , corresponding to the (111), (002) and (006) planes, which are consistent with the topology of the parent UiO-66-NH₂ [37] (Fig. 3c). In addition, the UiO-66-AM has a similar thermal stability to that of the UiO-66-NH₂ with an initial decomposition temperature of $\sim 370^\circ\text{C}$ and a significant mass loss of $\sim 50\%$ at $\sim 800^\circ\text{C}$ presumably due to the ligand decomposition (Fig. S3).

In the FTIR spectra, the main bands of the UiO-66-NH₂ are well retained in the UiO-66-AM, manifesting the stretching vibration of carboxyl groups at 1572 , 1433 and 1386 cm^{-1} , and the Zr-O stretching vibration at 769 and 665 cm^{-1} (Fig. 3d). The weakened absorption peak at 1257 cm^{-1} of the amino group in the UiO-66-AM is attributed to the formation of the secondary amido species at 3274 cm^{-1} . The appearance of the new C=C stretching vibration at 1656 cm^{-1} also verifies the acrylation modification. The main spectral features of UiO-66-AM can

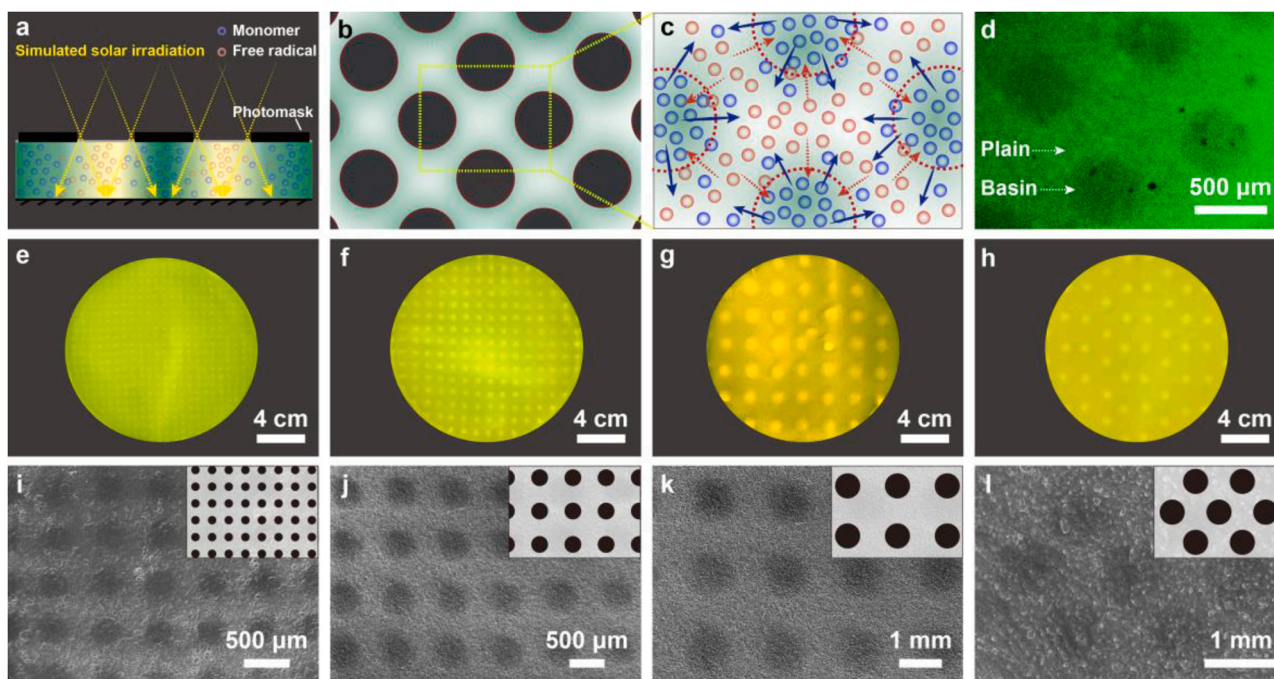


Fig. 2. (a-c) Schematic illustration of photopolymerization procedure of the patterned PNIPAM hydrogel, and the diffusion process of NIPAM monomers (blue solid arrows) and free radicals (orange dashed arrows). (d) CLSM image of patterned gel stained with Rhodamine B. (e-h) Optical images of patterned PHs with different basin sizes, and (i-l) SEM images of corresponding PGs. The insets in (i-l) are the schematics of corresponding masks.

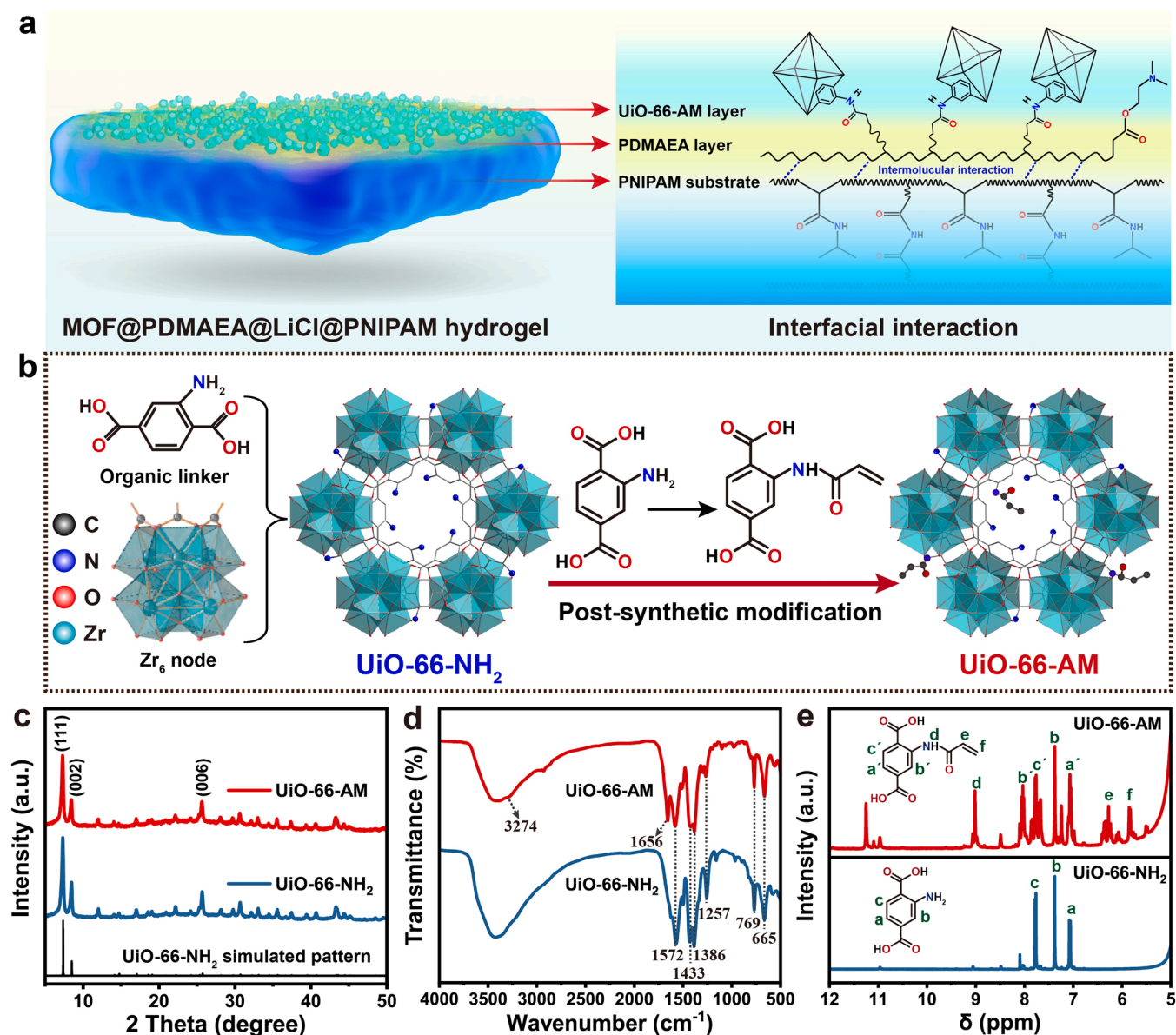


Fig. 3. Schematic diagrams of (a) spray-coating of MOF/PDMAEA onto the hydrogel surface, and (b) post-synthetic modification of UiO-66-NH₂ to UiO-66-AM. (c) XRD patterns, (d) FTIR spectra, and (e) ^1H NMR spectra of UiO-66-NH₂ and UiO-66-AM.

also be reflected clearly in its ^1H NMR spectrum with the new resonance peaks at 5.9, 6.3, 7.8, 8.1 and 9.1 ppm (Fig. 3e). On the basis of the integrated areas of the secondary amine proton at 9.1 ppm and the aromatic proton of the unreacted at 7.4 ppm H₂N-H₂BDC ligand, the calculated substitution of amine to amide is $\sim 30\%$. Generally, the modification occurs preferentially at the surface and the channel entrances in the framework, resulting in the partial substitution of -NH₂. Meanwhile, the UiO-66-AM has a BET surface area of 583 m² g⁻¹, lower than that of UiO-66-NH₂ (1046 m² g⁻¹), which is ascribed to the large pendant groups (Fig. S4).

3.3. Morphology and chemical structures of the MOF@PDMAEA@LiCl@PNIPAM gels

Fig. 4 shows SEM images and EDS mappings of the MOF@PDMAEA@LiCl@PNIPAM gels. The top-view SEM observation shows that the gel has a plain-and-basin structure with the basin size of ~ 500 μm , and the MOF nanoparticles are robustly anchored (Fig. 4a-c). The surface roughness of the basins increases with the MOF concentration in the

precursor, which can also be reflected in the SEM and AFM images of the MG (Fig. S5). The front-view SEM image presents the cross-sectional structure of the gel, exhibiting the basin with its depth of ~ 30 μm and the protruding MOFs (Fig. 4d-f). The observed interconnected PNIPAM skeleton is formed by the volume-exclusion effect of the vertically grown ice pillars during the bottom-up unidirectional-freezing process and subsequent freeze-drying [38,39]. The vertical pores of ~ 2 μm in width are clearly present in the side-view SEM images (Fig. 4g-i). The top-view and side-view elemental mapping images of the MG demonstrate the uniform distribution of Zr, C, N, and Cl elements (Fig. 4j-m). The integration of the MOF nanoparticles and the non-volatile PDMAEA base on the top of the gel would facilitate their utilization in catalytic hydrolysis of DMNP, and the directional microchannels on the side of the gel are beneficial to the absorption and transport of water molecules during the atmospheric water collection process.

Fig. 5 characterizes the chemical structures and compositions of PNIPAM gel, LiCl@PNIPAM gel, and MGs with different MOF loadings. In the FTIR spectra (Fig. 5a), the stretching vibration peaks of C-H at 3020, 2952 and 2890 cm⁻¹ are assigned to the PNIPAM skeleton, and

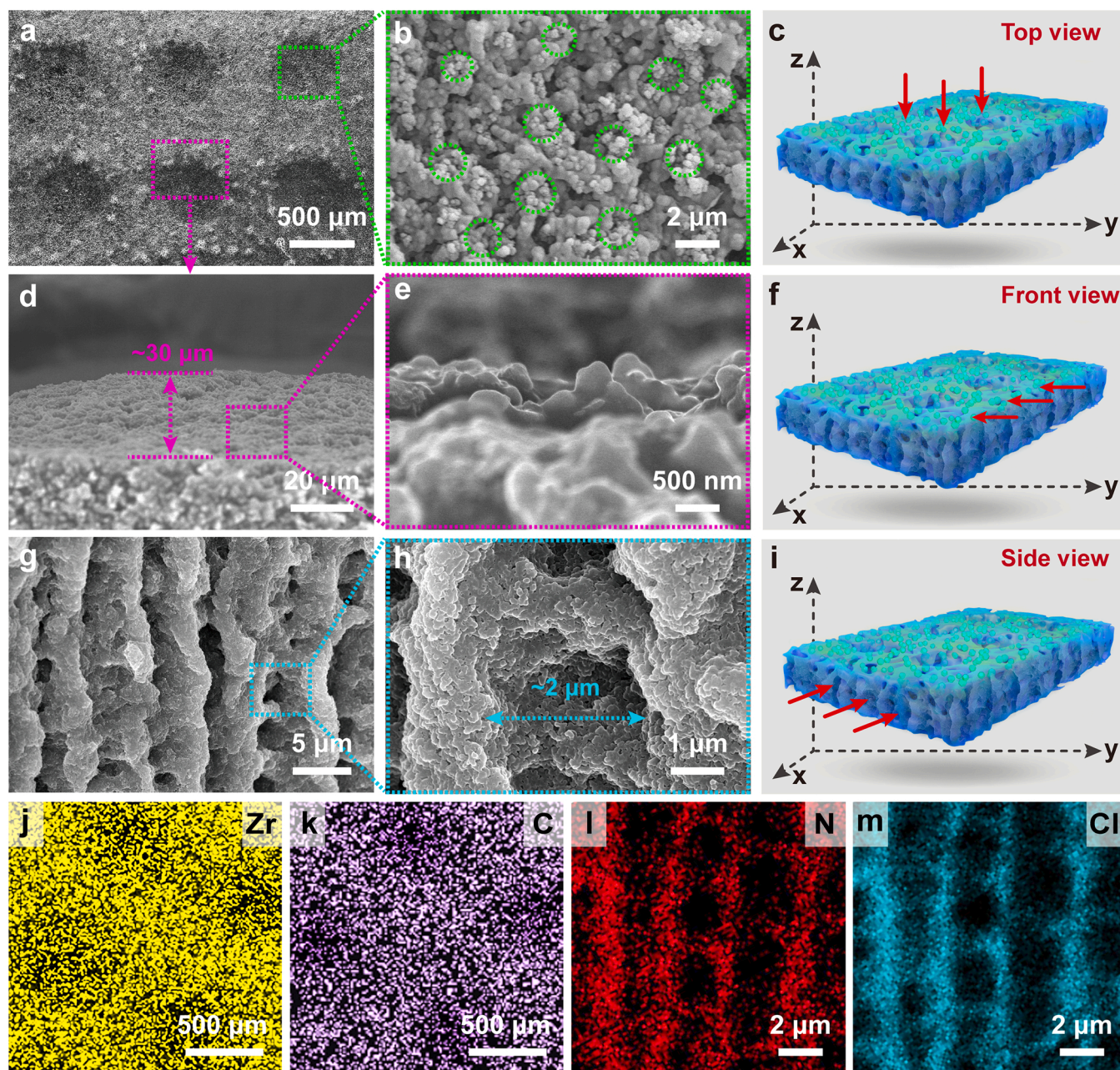


Fig. 4. (a, b) Top-view, (d, e) front-view, and (g, h) side-view SEM images of the MG and corresponding (c, f, i) schematic illustration of observation directions. (j, k) Top-view and (l, m) side-view elemental mapping images of Zr, C, N, and Cl elements of MG.

the adjacent doublets at 1388 and 1369 cm^{-1} derive from the vibration coupling splitting of the symmetric deformation of the dimethyl group of the isopropyl group [40]. After the salinization with LiCl, the amide I band detected at 1650 cm^{-1} shifts to a lower band, which is ascribed to the coordination of the lithium ions with the carbonyl groups [41]. The amide II band at 1548 cm^{-1} is inclined to combine with chloride anions and has a slight blue-shift [42]. Besides, the N-H shoulder peak of the secondary amido species at 3270 cm^{-1} is enhanced because of the coated PDMAEA. The unshared electron pair of oxygen in the C-O-C undergoes p- π conjugation with carbonyl groups, resulting in the asymmetrical and symmetrical stretching vibrations at the higher frequencies of 1172 and 1157 cm^{-1} . The XRD pattern of the MG (Fig. 5b) shows the broad peak of amorphous PNIPAM, and the typical MOF crystalline peaks at 7.34°, 8.52° and 25.68°, consistent with the results in Fig. 3c. The chemical states of the components of the gels are identified with their XPS spectra (Fig. 5c-e). As expected, the C 1 s, N 1 s, O

1 s, and Cl 2p signals are detected in the survey spectra of LG and MG. The C 1 s spectrum of MG-3 can be divided into three peaks at 284.6, 285.7 and 287.5 eV, corresponding to C-C, C-N and C=O bonds in the PNIPAM skeleton, respectively. The Zr 3d signal of the MG is distinct from the LG. As compared to that of the UiO-66-AM, the binding energies of Zr 3d_{3/2} and Zr 3d_{5/2} electrons in the MG-3 shift to 184.9 and 182.6 eV (Fig. S6).

In addition, the thermal stability and component content of the gels are analyzed on the basis of their TGA results (Fig. 5f). The two-step mass loss of the LG is ascribed to the removal of water molecules and the decomposition of the PNIPAM skeleton. The final residue at 800 °C is LiCl (~30%). The mass loadings of UiO-66-AM in MG-1, MG-2 and MG-3 are approximately 5.1, 8.5 and 13.2 wt%, respectively (Table S1). The concentration of Zr²⁺ in the MG is determined by the ICP-OES measurement, and the estimated MOF loadings ranged from 5.2 wt% to 12.1 wt%, consistent with the TGA results (Table S2).

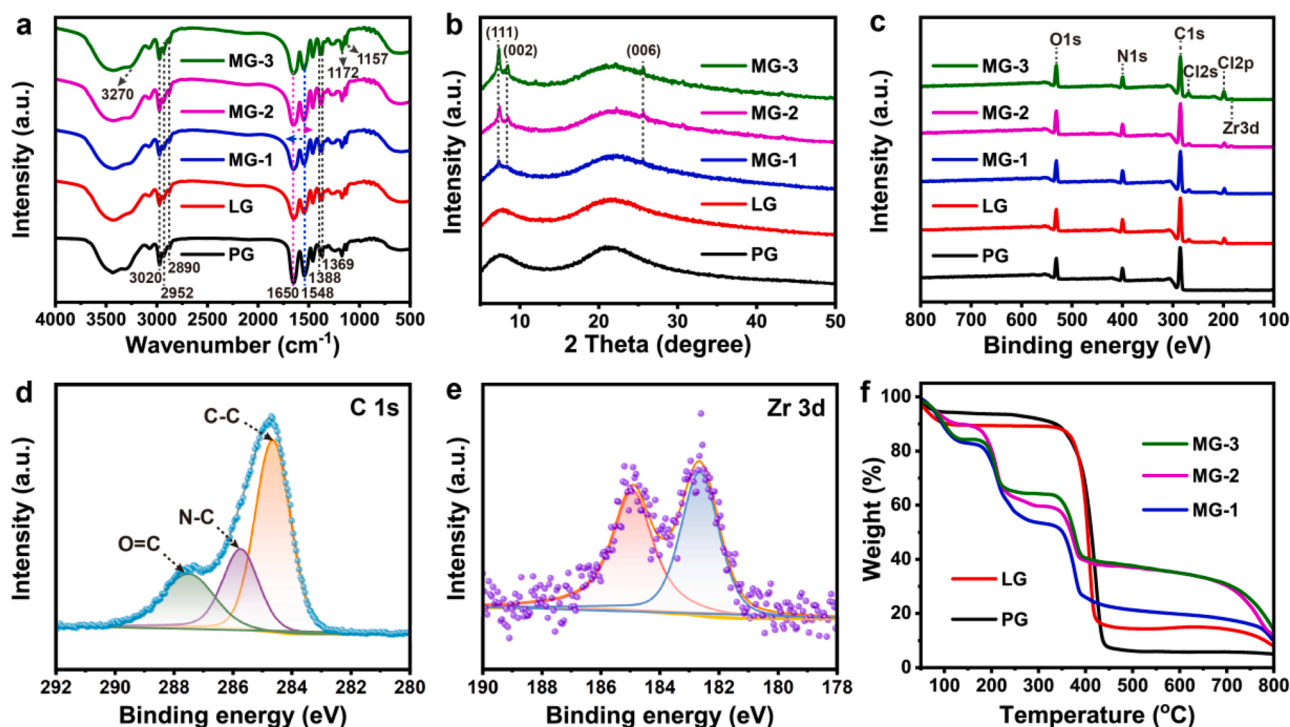


Fig. 5. (a) FTIR spectra, (b) XRD patterns, (c-e) XPS spectra, and (f) TGA curves of PG, LG, MG-1, MG-2, and MG-3.

3.4. Moisture absorption performances of the MOF@PDMAEA@LiCl@PNIPAM gels

To provide non-bulk water for the catalytic hydrolysis of DMNP in atmospheric environments, the moisture absorption performances of MGs are evaluated under a wide relative humidity range within 24 h. Fig. 6 shows the influences of the MOF loading and the relative humidity on water uptake of the gels. As reported [34], the moisture absorption process of a hygroscopic gel is subjected to a two-step water transfer. Firstly, the hygroscopic molecules convert the captured water molecules from the moist air to crystalline hydrates, which can condense on the gel surface; and the condensed droplets are subsequently absorbed gradually by the gel and stored in the gel networks (Fig. 6a). The moisture absorption capacity of the LG is up to 5.7 g g^{-1} at 90% RH, which is 119% higher than that of the RG without the directional microchannels (Fig. 6b, S7). The moisture absorption capacity of the CG is only 4.1 g g^{-1} , indicating that the construction of the three-dimensional structure of the gel facilitates the moisture absorption (Table S3). The MGs with different MOF loadings exhibit excellent moisture absorption capacities of 5.8, 6.2 and 6.4 g g^{-1} (Fig. 6b, S8) because the presence of MOF nanoparticles facilitates the adsorption and attachment of water molecules in moist air under high relative humidity condition. Under lower RH conditions, the MGs still exhibit satisfactory moisture absorption capacities (Fig. S9), while the relative moisture absorption performance (measured in grams per gram) of the MG is less than that of the LG due to the presence of the high-density MOF nanoparticles in the case of unsaturated hydration at 30% RH.

As shown in the 3D projection map (Fig. 6c), the RH variation influences water uptake of the gels, and the resulting vapor pressure difference drives the diffusion, transfer and hydration of water molecules to the hydrophilic groups of the polymer skeleton. To further evaluate the advantages of the MG as an efficient hygroscopic agent, the water collection amounts of the MGs are compared with those of reported inorganic salt-based hygroscopic materials (Fig. 6d), PAN/MIL@LiCl [43], PC-MOF [44], IPN gel [45], GO-SSNF [46], CaCl₂@UiO-66 [47], LiCl-UiO-66 [48], HCS@LiCl [49], and LiCl@HGAFs [50]. It is seen that the super-hygroscopic MGs exhibit excellent moisture absorption

performances over a wide RH range, benefiting from the hierarchical integration of the MOF catalyst and the PDMAEA base on the super-hygroscopic LiCl@PNIPAM gel substrate with a plain-and-basin structure and numerous directional microchannels.

The optical images of LG and MG show the gel transformation from aerogel state to hydrogel state with a surrounding water envelope after water uptake (Fig. 6e). The hygroscopic efficiency of the gels can be expressed as a function of the saturated water content (Q_s) with time (Fig. 6f, Table S4). In the first stage of the hydration, the rapidly trapped water molecules in the MG need $\sim 500 \text{ min}$ to reach 80% hydration, which is $\sim 95 \text{ min}$ faster than the LG. The corresponding water contents in MG and LG are 5.1 and 4.5 g g^{-1} , respectively, indicating that the presence of MOFs also promotes the liquefaction of water molecules. In addition, the moisture absorption capacity of the MG maintains more than 91% (4.1 g g^{-1}) of its initial value after five cycles at 90% RH for 5 h, higher than that of the LG (85%, 3.1 g g^{-1}), revealing stable cyclic performances of the MG (Fig. 6g). The XRD patterns of MG and LG in Fig. S10 after the absorption-desorption cycling tests are consistent with those of the samples before the water uptake (Fig. 5b).

Usually, in a hydrated polymer network, there are strong hydrogen bonding interactions between water molecules and the hydrophilic PNIPAM chains, and these water molecules have weak interactions with surrounding ones, resulting in water clusters encapsulated in the polymer network [51,52]. The state of the water molecules inside the MG after the hydration for 5 h is revealed with the Raman spectrum (Fig. 6h), and the region of O-H stretching is fitted by the Gaussian function. The peaks at 3225 and 3395 cm^{-1} are related to free water (FW) consisting of two protons and two lone electron pairs that are involved in hydrogen bonding [53–55], while the peaks at 3479 and 3591 cm^{-1} derive from the stretching vibrations of weakly hydrogen-bonded water molecules of intermediate water (IW) [56–58]. These weakly bonded water molecules could generate hydration shells surrounding the PNIPAM skeleton, which can continuously provide water for the catalytic hydrolysis of DMNP in atmospheric environments.

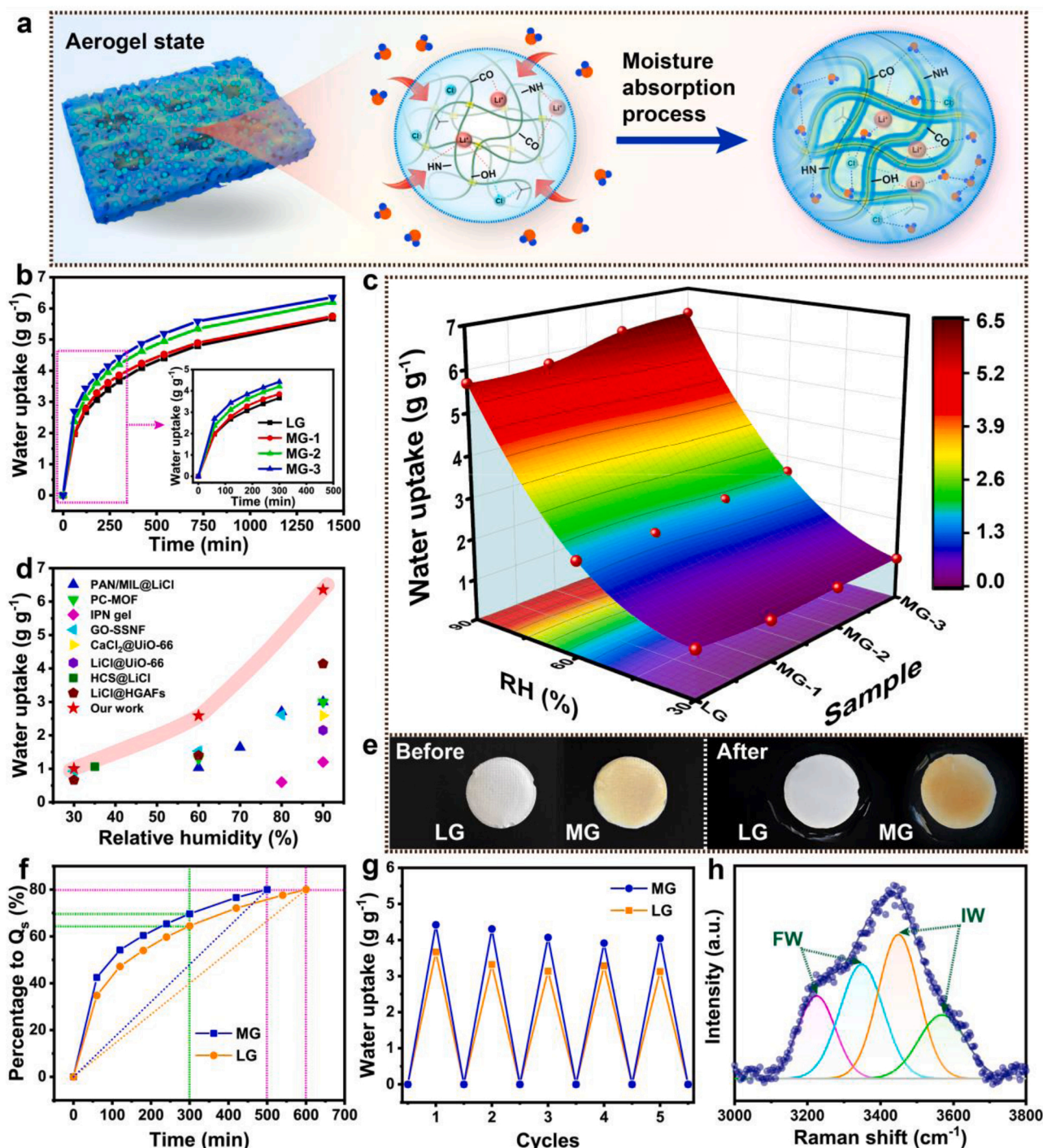


Fig. 6. (a) Schematic illustration of the hygroscopic process of the gel. (b) Plots of water uptake for LG, MG-1, MG-2, and MG-3 at 90% RH. (c) 3D projection map of the moisture absorption capacity versus relative humidity of MGs. (d) Comparison of moisture absorption capacity of hygroscopic materials. (e) Optical images of LG and MG before and after the moisture absorption. (f) Percentages to the saturated water content (Q_s) with time for LG and MG. (g) Absorption-desorption cyclic stability of LG and MG at 90% RH for 5 h (absorption at 25 °C and desorption at 100 °C). (h) Raman spectrum of MG with 80% of hydration.

3.5. Catalytic hydrolysis of DMNP by UiO-66-AM and UiO-66-NH₂ in liquid-phase

Considering the high risk of using real nerve agents (tabun, sarin, soman and VX), DMNP with a similar chemical structure to soman is chosen for its catalytic hydrolysis. In view of the high difficulty in the DMNP hydrolysis without bulk water, the catalytic activity of the Zr-MOF is usually evaluated in liquid phase in the literature. For comparison, the catalytic hydrolysis of DMNP with the synthesized MOF

powders is carried out in liquid-phase. On the basis of the reaction shown in Fig. 7a, the P-O bond in the DMNP can be cleaved to generate dimethyl phosphate (DMP) and *p*-nitrophenol (4-NP). The catalytic hydrolysis reactions of DMNP with UiO-66-AM and UiO-66-NH₂ in the N-ethylmorpholine (NEM, 0.45 M, pH 10.5) buffer are monitored by the UV-vis spectra, and the enhanced peak of 4-NP appears at 402 nm in Fig. S11. The organophosphorus compounds are detected by the ³¹P NMR spectroscopy with the attenuated peak of DMNP at -4.4 ppm and the enhanced peak of DMP at 2.8 ppm at 0, 3, 10 and 60 min,

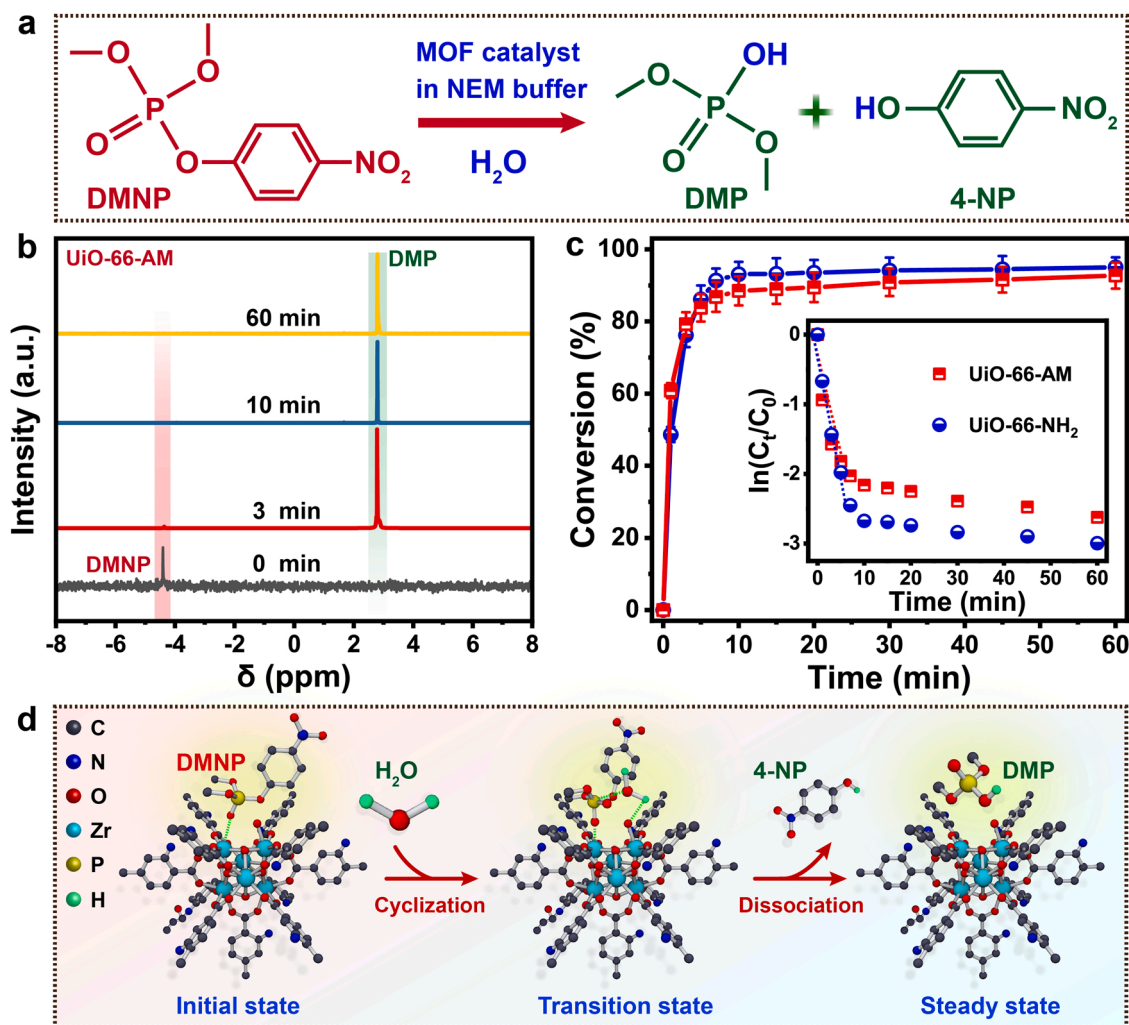


Fig. 7. (a) Reaction process of MOF-catalyzed hydrolysis of DMNP in the NEM buffer. (b) ^{31}P NMR spectra of hydrolysis products at 0, 3, 10, and 60 min. (c) Conversion profiles of DMNP by UiO-66-AM and UiO-66-NH₂ with inserted kinetic profiles. (d) Reaction mechanism and corresponding states of the DMNP hydrolysis catalyzed by UiO-66-AM.

respectively (Fig. 7b).

Based on the first-order kinetics, the initial half-life of the UiO-66-AM (2.6 min) is comparable to that of its parent UiO-66-NH₂ (2.0 min), and corresponding initial turnover frequencies (TOFs) are 0.068 and 0.052 s⁻¹, respectively. Meanwhile, more than 88% of the DMNP can be hydrolyzed by the UiO-66-NH₂ and the UiO-66-AM within 10 min, demonstrating their high conversion efficiencies and rates (Fig. 7c). These results indicate that the post-synthetic modification shows slight influence on the catalytic activity of the UiO-66-AM in the liquid-phase. Moreover, the hydrolysis rate of the DMNP by the UiO-66-AM in the DMAEA buffer is retarded obviously ($t_{1/2} \sim 1.8$ h), while the conversion still exceeds 90% within 24 h (Fig. S12).

In general, the hydrolysis process of DMNP is highly dependent on the type of alkaline buffer and the amount of water equivalent [59]. In the liquid-phase reactions, stronger alkaline buffers are more conducive to promoting the formation of non-toxic product via the hydrolysis pathway [60,61]. However, the generated acidic product may retard the reaction progress if the amount of base is insufficient [62]. Moreover, the nitrogen-heterocyclic organic compound of NEM is prone to combine with the acidic product (4-NP) and accelerates the reaction, while the DMAEA may only serve as a proton acceptor and results in a relatively slow reaction rate. Fig. 7d explores the potential hydrolysis mechanism of DMNP by the MOFs. The P=O moiety in the organophosphate is captured by the defective Zr₆ node with missing linker on

the framework acted as the active site [63]. The hydrogen bonds can be formed between the DMNP and adjacent node-ligated water molecules, while the π - π stacking interactions between the phenyl ring of the DMNP and the benzene ring of the linker on the framework enhance the hydrogen bonding stability [64]. The nucleophilic attack on the organophosphate by the -OH group provided by the alkaline buffer, followed by the cleavage of P-O bonds and the dissociation of the hydrolysis product.

3.6. Catalytic hydrolysis of DMNP by the MG in atmospheric environments

Inspired by the positive moisture absorption and the catalytic hydrolysis performances in liquid-phase, the catalytic destruction of DMNP by the super-hygroscopic MG microreactor is explored in solid-phase under different relative humidities. After dropping the target DMNP onto the surface, the MG microreactor is immediately put in a chamber at a constant temperature of 25 °C under the RH of 90% for simultaneous moisture absorption and catalytic hydrolysis. As the target diffuses to the nearby catalytic sites, the absorbed water molecules condensed into the droplets on the MG surface. An accelerated reaction microenvironment is constructed with the DMNP target, the MOF catalyst, the non-volatile polymer base, and the water derived from the moist air (Fig. 8a). The trapped DMNP molecule forms a fragile

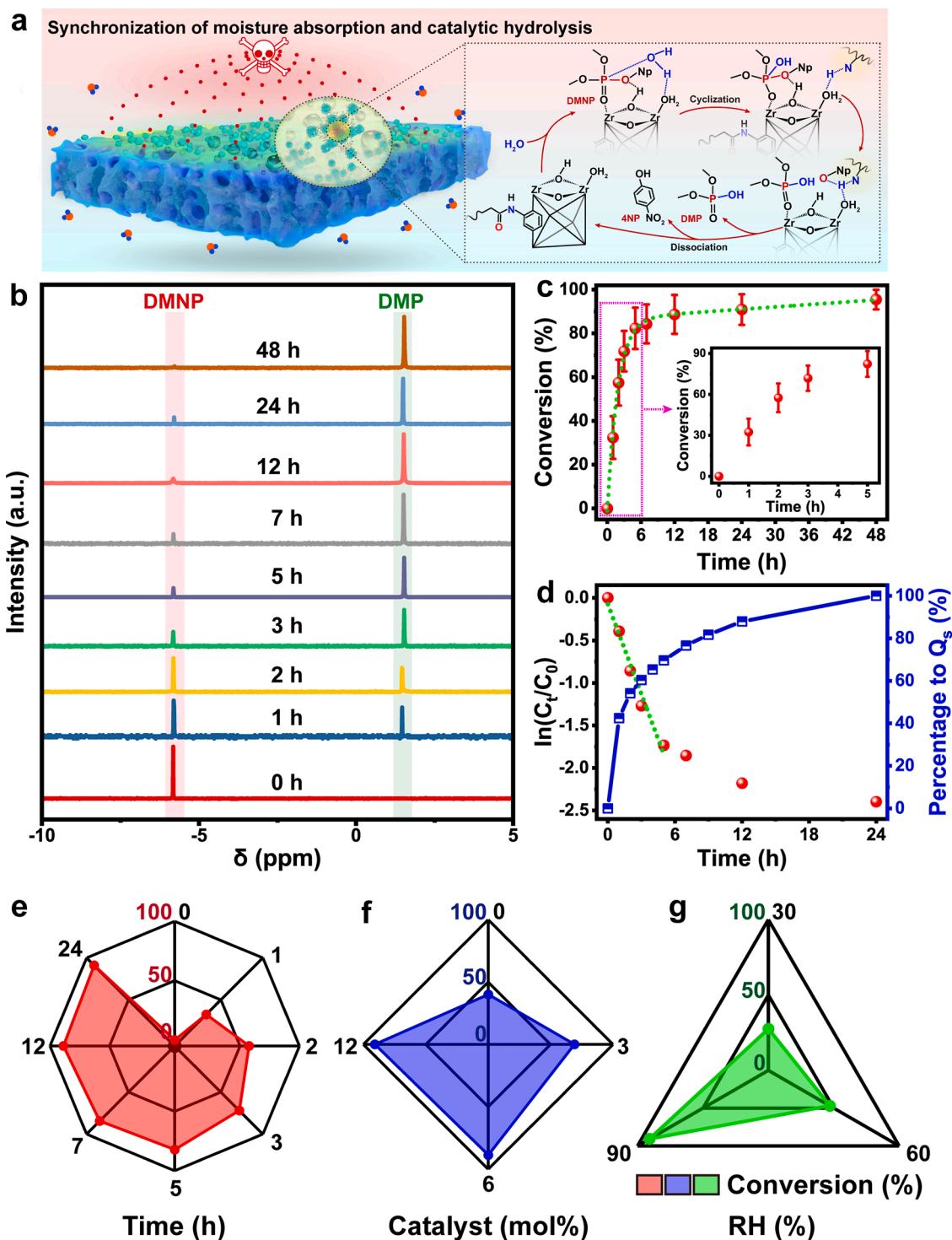


Fig. 8. (a) Schematic illustration of the catalytic degradation of DMNP by MG in the moist air. (b) ^{31}P NMR spectra for monitoring the reaction process at 90% RH. (c) Plots of conversion rate as a function of time. (d) Kinetic fitting profile and the percentages to the saturated water content over time. (e–g) Effects of time, MOF content and RH on the conversions.

pentacoordinate phosphorus intermediate with the Zr-node, which is attacked by the non-bulk water molecules and further decomposed to benign products with the help of proton transfer by the proximal polymer base. Fig. 8b monitors the dynamic process of the destruction reaction at 90% RH by the ^{31}P NMR spectra. The peak at ~ 1.2 ppm for the DMP product appears and increases in intensity as a function of the reaction time, while the peak at approximately -5.8 ppm for the DMNP decreases. According to the ratio of the integrated areas, the conversion

rate is $\sim 57.5\%$ in 2 h (Fig. 8c), which is comparable to the results of the MOF powder in liquid-phase ($\sim 60\%$, Fig. S12). The presence of the benign products catalyzed by the MG for 2 h is further confirmed by the MS analysis in positive and negative modes (Fig. S13). More than 80% of the target is converted to benign products in 5 h and the conversion is up to 95.5% in 48 h, indicating the satisfied catalytic hydrolysis performance of DMNP by the MG microreactor under atmospheric conditions.

For comparison, the conversions of DMNP by LG, UiO-66-AM and

DMAEA as background reactions under single and pairwise combination conditions are shown in Fig. S14 and S15. Few products are observed when using LG, MOF or LG/MOF as the catalysts in 48 h, indicating that they have no apparent catalytic effect in the absence of the alkaline PDMAEA even at a high relative humidity of 90%. In the absence of the hygroscopic LG substrate, only 40% of DMNP is destructed by the MOF/DMAEA and converted to benign products by the nucleophilic attack in the phosphorus center for the P-O cleavage. In the absence of the MOF catalyst, the DMNP on the DMAEA and LG/DMAEA is decomposed to the toxic by-product M4NP via the C-O bond cleavage pathway (Fig. S16). In addition, the conversion rates of DMNP catalyzed by MG-1, MG-2 and MG-3 at 90% RH in 48 h are 69%, 88.8% and 95.5%, respectively (Fig. S17). These results verify the importance of the integrated microreactor for achieving efficient catalytic hydrolysis of DMNP and obtaining benign products under humidity conditions. Meanwhile, the number, size and depth of the basins influence the anchoring and dispersion of the MOF nanoparticles, and thus the catalytic efficiency (Fig. S18).

The dual-factor function curves (Fig. 8d) further indicate that the initial reaction rate constant and half-life ($t_{1/2}$) calculated from the first-order kinetic equation are closely related to the catalyst dosage and the saturated water content of the MG. The kinetic profile reveals the initial rate constant of 0.365 h^{-1} and the corresponding $t_{1/2}$ of 1.9 h, at which the microreactor provides up to 3.5 g g^{-1} water from the moist air for the DMNP hydrolysis, benefiting from the unique plain-and-basin structure with directional water transport microchannels. Furthermore, the cyclic catalytic performance of the MG for DMNP hydrolysis at 90% RH for 5 h is shown in Fig. S19a. The conversion of the MG-catalyzed DMNP hydrolysis could be maintained at 90.6% of the initial value after 5 cycles at 90% RH. It means that still more than 74% of the DMNP can be digested within 5 h after 5 cycles. The residual degradation products in the MG may partially block the path of the DMNP to the catalytic sites, resulting in the decrease in catalytic efficiency. The diffraction peaks of the MG are retained in the XRD pattern even after 5 catalytic cycles (Fig. S19b). It is speculated that the actual catalytic activity is more impressive because the number of the active sites is just a fraction of the catalyst loading.

Under lower relative humidity conditions, both the moisture absorption capacity and the hydration rate of MG are weakened. Nevertheless, the conversions of the benign products still reach 60% and 27.5% at 60% and 30% RH in 48 h, respectively (Fig. S20, S21). In addition, the effect of temperature on the conversion of DMNP by the MG can be influenced by several factors, such as the moisture absorption, the water evaporation, and the reaction rate constant (Fig. S22). The effects of the humidity dependence and the catalyst loading during the DMNP hydrolysis are illustrated via the radar maps (Fig. 8e-f). In the case of sufficient water molecules involved in the reaction, the presence of the MOF catalyst is a key factor in the formation of benign products, depending on the selectivity of the nucleophilic attack. Conversely, if the water content is insufficient, the catalytic reaction cannot be effectively accelerated despite the presence of both the catalyst and the base. These results demonstrate the significance of our design of integrating the MOF catalyst, the non-volatile polymer base, and the non-bulk water in one microreactor with plain-and-basin structure and directional microchannels.

4. Conclusions

To achieve efficient detoxification of the organophosphorus-containing nerve agent simulant in atmospheric environments, the spontaneously super-hygroscopic MOF@PDMAEA@LiCl@PNIPAM gel microreactors are constructed by the unique integration of the super-hygroscopic component, the MOF catalyst, the polymeric base, and the patterned PNIPAM gel substrate with plain-and-basin structure and numerous directional microchannels. The MG microreactor exhibits excellent spontaneous hygroscopicity, fast mass transport, and

satisfactory catalytic hydrolysis performances over a wide range of relative humidity because of the 3D gel substrate and the hierarchical integration for thorough exposure of the catalysts. Especially, the highly open microchannels are conducive to the absorption, transport and storage of water molecules, and the presence of MOF catalyst in the MG also facilitates the attachment of water molecules in moist air, exhibiting a moisture absorption capacity of up to 6.4 g g^{-1} at 90% RH. The integrated microreactor with thoroughly exposed MOF catalyst, rich non-bulk water, and non-volatile polymeric base exhibits high catalytic rate and activity towards the detoxification of DMNP with the initial half-life of 1.9 h and the final conversion of 95.5% under humidity conditions. Moreover, the UiO-66-AM with acrylamide moiety by post-synthetic modification still maintains a fast conversion efficiency in liquid-phase with a $t_{1/2}$ of 2.6 min and more than 88% conversion in 10 min. Furthermore, the hydrolysis mechanism of DMNP is explored regarding the selective cleavage of DMNP attacked by the non-bulk water provided by the MG microreactor to benign products and the synergistic catalysis of proximal PDMAEA base for achieving detoxification under atmospheric conditions. This work demonstrates a feasible design of spontaneously hygroscopic MOF-gel microreactors for efficient detoxification of lethal nerve agents and simulants in atmospheric environments.

CRediT authorship contribution statement

Xuejiao Wang: Methodology, Investigation, Data curation, Formal Analysis, Writing-Original Draft Preparation; **Jing Yang:** Formal Analysis, Writing-Reviewing and Editing; **Ming Zhang:** Characterization; **Qian Hu:** Investigation; **Bai-Xue Li:** Formal Analysis; **Jin Qu:** Methodology; **Zhong-Zhen Yu:** Supervision, Writing-Reviewing and Editing; **Dongzhi Yang:** Supervision, Funding Acquisition, Writing-Reviewing and Editing.

Declaration of Competing Interest

The authors declare that they have no known competing financial interests or personal relationships that could have appeared to influence the work reported in this paper.

Data Availability

Data will be made available on request.

Acknowledgements

Financial support from the National Natural Science Foundation of China (51972015, 52090034, 52221006) and the Fundamental Research Funds for the Central Universities (XK1802-2) is gratefully acknowledged.

Appendix A. Supporting information

Supplementary data associated with this article can be found in the online version at doi:10.1016/j.apcatb.2023.122516.

References

- [1] Y.L. Liao, W.K. Chen, S.Z. Li, W.L. Jiao, Y. Si, J.Y. Yu, B. Ding, Ultrathin zirconium hydroxide nanosheet-assembled nanofibrous membranes for rapid degradation of chemical warfare agents, *Small* 17 (2021) 2101639, <https://doi.org/10.1002/smll.202101639>.
- [2] K. Kim, O.G. Tsay, D.A. Atwood, D.G. Churchill, Destruction and detection of chemical warfare agents, *Chem. Rev.* 111 (2011) 5345–5403, <https://doi.org/10.1021/cr100193y>.
- [3] V.G. Snider, C.L. Hill, Functionalized reactive polymers for the removal of chemical warfare agents: a review, *J. Hazard. Mater.* 442 (2023) 130015, <https://doi.org/10.1016/j.jhazmat.2022.130015>.

- [4] S. Balasubramanian, A.J. Kulandaisamy, K.J. Babu, A. Das, J.B. Balaguru Rayappan, Metal organic framework functionalized textiles as protective clothing for the detection and detoxification of chemical warfare agents-a review, *Ind. Eng. Chem. Res.* 60 (2021) 4218–4239, <https://doi.org/10.1021/acs.iecr.0c06096>.
- [5] T. Islamoglu, Z. Chen, M.C. Wasson, C.T. Buru, K.O. Kirlikovali, U. Afrin, M. R. Mian, O.K. Farha, Metal-organic frameworks against toxic chemicals, *Chem. Rev.* 120 (2020) 8130–8160, <https://doi.org/10.1021/acs.chemrev.9b00828>.
- [6] H.-B. Luo, A.J. Castro, M.C. Wasson, W. Flores, O.K. Farha, Y. Liu, Rapid, biomimetic degradation of a nerve agent simulant by incorporating imidazole bases into a metal-organic framework, *ACS Catal.* 11 (2021) 1424–1429, <https://doi.org/10.1021/acscatal.0c04565>.
- [7] H.L. Liu, N.Y. Li, M.Y. Feng, G.Y. Li, W.P. Zhang, T.C. An, Near-infrared light induced adsorption-desorption cycle for VOC recovery by integration of metal-organic frameworks with graphene oxide nanosheets, *Environ. Sci. Nano* 9 (2022) 1858–1868, <https://doi.org/10.1039/D2EN00103A>.
- [8] H.L. Liu, M.J. Xu, G.Y. Li, W.P. Zhang, T.C. An, Solar-light-triggered regenerative adsorption removal of styrene by silver nanoparticles incorporated in metal-organic frameworks, *Environ. Sci. Nano* 8 (2021) 543–553, <https://doi.org/10.1039/D0EN01011A>.
- [9] X. Ding, H.L. Liu, J.Y. Chen, M.C. Wen, G.Y. Li, T.C. An, H.J. Zhao, In situ growth of well-aligned Ni-MOF nanosheets on nickel foam for enhanced photocatalytic degradation of typical volatile organic compounds, *Nanoscale* 12 (2020) 9462–9470, <https://doi.org/10.1039/D0NR01027H>.
- [10] H.L. Liu, X.Y. Chang, X.X. Liu, G.Y. Li, W.P. Zhang, T.C. An, Boosting the photocatalytic degradation of ethyl acetate by a Z-scheme Au-TiO₂@NH₂-UiO-66 heterojunction with ultrafine Au as an electron mediator, *Environ. Sci. Nano* 8 (2021) 2542–2553, <https://doi.org/10.1039/D1EN00225B>.
- [11] M.C. Wen, G.Y. Li, H.L. Liu, J.Y. Chen, T.C. An, H. Yamashita, Metal-organic framework-based nanomaterials for adsorption and photocatalytic degradation of gaseous pollutants: recent progress and challenges, *Environ. Sci. Nano* 6 (2019) 1006–1025, <https://doi.org/10.1039/C8EN01167B>.
- [12] L. Wang, J. Mao, G. Huang, Y. Zhang, J. Huang, H. She, C. Liu, H. Liu, Q. Wang, Configuration of hetero-framework via integrating MOF and triazine-containing COF for charge-transfer promotion in photocatalytic CO₂ reduction, *Chem. Eng. J.* 446 (2022), 137011, <https://doi.org/10.1016/j.cej.2022.137011>.
- [13] L. Wang, Z. Liu, J. Zhang, Y. Jia, J. Huang, Q. Mei, Q. Wang, Boosting charge separation of BiVO₄ photoanode modified with 2D metal-organic frameworks nanosheets for high-performance photoelectrochemical water splitting, *Chin. Chem. Lett.* (2023), 108007, <https://doi.org/10.1016/j.ccl.2022.108007>.
- [14] M.J. Katz, J.E. Mondloch, R.K. Totten, J.K. Park, S.T. Nguyen, O.K. Farha, J. T. Hupp, Simple and compelling biomimetic metal-organic framework catalyst for the degradation of nerve agent simulants, *Angew. Chem. Int. Ed.* 53 (2014) 497–501, <https://doi.org/10.1002/ange.201307520>.
- [15] A.M. Ploskonka, J.B. DeCoste, Insight into organophosphate chemical warfare agent simulant hydrolysis in metal-organic frameworks, *J. Hazard. Mater.* 375 (2019) 191–197, <https://doi.org/10.1016/j.jhazmat.2019.04.044>.
- [16] S.Y. Moon, Y.Y. Liu, J.T. Hupp, O.K. Farha, Instantaneous hydrolysis of nerve-agent simulants with a six-connected zirconium-based metal-organic framework, *Angew. Chem. Int. Ed.* 54 (2015) 6795–6799, <https://doi.org/10.1002/ange.201502155>.
- [17] M.J. Katz, R.C. Klet, S.Y. Moon, J.E. Mondloch, J.T. Hupp, O.K. Farha, One step backward is two steps forward: enhancing the hydrolysis rate of UiO-66 by decreasing [OH⁻], *ACS Catal.* 5 (2015) 4637–4642, <https://doi.org/10.1021/acscatal.5b00785>.
- [18] K.O. Kirlikovali, Z. Chen, T. Islamoglu, J.T. Hupp, O.K. Farha, Zirconium-based metal-organic frameworks for the catalytic hydrolysis of organophosphorus nerve agents, *ACS Appl. Mater. Interfaces* 12 (2020) 14702–14720, <https://doi.org/10.1021/acsami.9b20154>.
- [19] M.J. Katz, S.-Y. Moon, J.E. Mondloch, M.H. Beyzavi, C.J. Stephenson, J.T. Hupp, O. K. Farha, Exploiting parameter space in MOFs: a 20-fold enhancement of phosphate-ester hydrolysis with UiO-66-NH₂, *Chem. Sci.* 6 (2015) 2286–2291, <https://doi.org/10.1039/C4SC03613A>.
- [20] L.N. Song, T.Y. Zhao, D.Z. Yang, X.J. Wang, X.M. Hao, Y.X. Liu, S.Y. Zhang, Z.-Z. Yu, Photothermal graphene/UiO-66-NH₂ fabrics for ultrafast catalytic degradation of chemical warfare agent simulants, *J. Hazard. Mater.* 393 (2020), 122332, <https://doi.org/10.1016/j.jhazmat.2020.122332>.
- [21] K. Vellingiri, L. Philip, K.-H. Kim, Metal-organic frameworks as media for the catalytic degradation of chemical warfare agents, *Coord. Chem. Rev.* 353 (2017) 159–179, <https://doi.org/10.1016/j.ccr.2017.10.010>.
- [22] S.J. Garibay, O.K. Farha, J.B. DeCoste, Single-component frameworks for heterogeneous catalytic hydrolysis of organophosphorus compounds in pure water, *Chem. Commun.* 55 (2019) 7005–7008, <https://doi.org/10.1039/C9CC02236H>.
- [23] K.Y. Cho, J.Y. Seo, H.-J. Kim, S.J. Pai, X.H. Do, H.G. Yoon, S.S. Hwang, S.S. Han, K.-Y. Baek, Facile control of defect site density and particle size of UiO-66 for enhanced hydrolysis rates: insights into feasibility of Zr(IV)-based metal-organic framework (MOF) catalysts, *Appl. Catal. B* 245 (2019) 635–647, <https://doi.org/10.1016/j.apcatb.2019.01.033>.
- [24] Z. Chen, T. Islamoglu, O.K. Farha, Toward base heterogenization: a zirconium metal-organic framework/dendrimer or polymer mixture for rapid hydrolysis of a nerve-agent simulant, *ACS Appl. Nano Mater.* 2 (2019) 1005–1008, <https://doi.org/10.1021/acsanm.8b02292>.
- [25] S.Y. Moon, E. Prousaloglou, G.W. Peterson, J.B. DeCoste, M.G. Hall, A.J. Howarth, J.T. Hupp, O.K. Farha, Detoxification of chemical warfare agents using a Zr-6-based metal-organic framework/polymer mixture, *Chem. Eur. J.* 22 (2016) 14864–14868, <https://doi.org/10.1002/chem.201603976>.
- [26] Z.J. Chen, P.H. Li, X.J. Wang, K.-I. Otake, X. Zhang, L. Robison, A. Atilgan, T. Islamoglu, M.G. Hall, G.W. Peterson, J.F. Stoddart, O.K. Farha, Ligand-directed reticular synthesis of catalytically active missing zirconium-based metal-organic frameworks, in: *J. Am. Chem. Soc.*, 2019, pp. 12229–12235, <https://doi.org/10.1021/jacs.9b06179>.
- [27] M.R. Mian, T. Islamoglu, U. Afrin, S. Goswami, R. Cao, K.O. Kirlikovali, M.G. Hall, G.W. Peterson, O.K. Farha, Catalytic degradation of an organophosphorus agent at Zn-OH sites in a metal-organic framework, *Chem. Mater.* 32 (2020) 6998–7004, <https://doi.org/10.1021/acs.chemmater.0c02373>.
- [28] Z. Chen, K. Ma, J.J. Mahle, H. Wang, Z.H. Syed, A. Atilgan, Y. Chen, J.H. Xin, T. Islamoglu, G.W. Peterson, O.K. Farha, Integration of metal-organic frameworks on protective layers for destruction of nerve agents under relevant conditions, *J. Am. Chem. Soc.* 141 (2019) 20016–20021, <https://doi.org/10.1021/jacs.9b11172>.
- [29] J.Y. Seo, M.H. Choi, B.W. Lee, J.-H. Lee, S. Shin, S. Cho, K.Y. Cho, K.-Y. Baek, Feasible detoxification coating material for chemical warfare agents using poly(methyl methacrylate)-branched poly(ethyleneimine) copolymer and metal-organic framework composites, *ACS Appl. Mater. Interfaces* 14 (2022) 50246–50255, <https://doi.org/10.1021/acsami.2c15961>.
- [30] H. Wang, J.J. Mahle, T.M. Tovar, G.W. Peterson, M.G. Hall, J.B. DeCoste, J. H. Buchanan, C.J. Karwacki, Solid-phase detoxification of chemical warfare agents using zirconium-based metal organic frameworks and the moisture effects: analyze via digestion, *ACS Appl. Mater. Interfaces* 11 (2019) 21109–21116, <https://doi.org/10.1021/acsami.9b04927>.
- [31] Y.H. Guo, W.X. Guan, C.X. Lei, H.Y. Lu, W. Shi, G.H. Yu, Scalable super hygroscopic polymer films for sustainable moisture harvesting in arid environments, *Nat. Commun.* 13 (2022) 2761, <https://doi.org/10.1038/s41467-022-30505-2>.
- [32] W. Yao, X. Zhu, Z. Xu, R.A. Davis, G. Liu, H. Zhong, X. Lin, P. Dong, M. Ye, J. Shen, Loofah sponge-derived hygroscopic photothermal absorber for all-weather atmospheric water harvesting, *ACS Appl. Mater. Interfaces* 14 (2022) 4680–4689, <https://doi.org/10.1021/acsami.1c20576>.
- [33] D. Ma, P. Li, X. Duan, J. Li, P. Shao, Z. Lang, L. Bao, Y. Zhang, Z. Lin, B. Wang, A hydrolytically stable vanadium(IV) metal-organic framework with photocatalytic bacteriostatic activity for autonomous indoor humidity control, *Angew. Chem. Int. Ed.* 59 (2020) 3905–3909, <https://doi.org/10.1002/anie.201914762>.
- [34] X.J. Wang, D.Z. Yang, M. Zhang, Q. Hu, K.J. Gao, J.S. Zhou, Z.-Z. Yu, Super-hygroscopic calcium chloride/graphene oxide/poly(N-isopropylacrylamide) gels for spontaneous harvesting of atmospheric water and solar-driven water release, *ACS Appl. Mater. Interfaces* 14 (2022) 33881–33891, <https://doi.org/10.1021/acsami.2c08591>.
- [35] H. Kim, S.J. Lee, Stomata-inspired membrane produced through photopolymerization patterning, *Adv. Funct. Mater.* 25 (2015) 4496–4505, <https://doi.org/10.1002/adfm.201501445>.
- [36] M. Guvendiren, J.A. Burdick, S. Yang, Solvent induced transition from wrinkles to creases in thin film gels with depth-wise crosslinking gradients, *Soft Matter* 6 (2010) 5795–5801, <https://doi.org/10.1039/C0SM00317D>.
- [37] J.H. Cavka, S. Jakobsen, U. Olsbye, N. Guillou, C. Lamberti, S. Bordiga, K. P. Lillerud, A new zirconium inorganic building brick forming metal organic frameworks with exceptional stability, *J. Am. Chem. Soc.* 130 (2008) 13850–13851, <https://doi.org/10.1021/ja8057953>.
- [38] X.-H. Li, P.F. Liu, X. Li, F. An, P. Min, K.-N. Liao, Z.-Z. Yu, Vertically aligned, ultrathin and highly compressive all-graphitized graphene aerogels for highly thermally conductive polymer composites, *Carbon* 140 (2018) 624–633, <https://doi.org/10.1016/j.carbon.2018.09.016>.
- [39] L. Qiu, J.Z. Liu, S.L.Y. Chang, Y.Z. Wu, D. Li, Biomimetic superelastic graphene-based cellular monoliths, *Nat. Commun.* 3 (2012) 1214, <https://doi.org/10.1038/ncomms2251>.
- [40] B. Kim, J.-S. Lee, Thermally reversible shape transformation of nano-patterned PNIPAAm hydrogel, *Polym. Bull.* 78 (2020) 3353–3361, <https://doi.org/10.1007/s00289-020-03276-3>.
- [41] H.I. Okur, J. Kherb, P.S. Cremer, Cations bind only weakly to amides in aqueous solutions, *J. Am. Chem. Soc.* 135 (2013) 5062–5067, <https://doi.org/10.1021/ja3119256>.
- [42] Y. Zhang, S. Furryk, L.B. Sagle, Y. Cho, D.E. Bergbreiter, P.S. Cremer, Effects of hofmeister anions on the LCST of PNIPAM as a function of molecular weight, *J. Phys. Chem. C* 111 (2007) 8916–8924, <https://doi.org/10.1021/jp0606003>.
- [43] Y. Zhang, L. Wu, X. Wang, J. Yu, B. Ding, Super hygroscopic nanofibrous membrane-based moisture pump for solar-driven indoor dehumidification, *Nat. Commun.* 11 (2020) 3302, <https://doi.org/10.1038/s41467-020-17118-3>.
- [44] G. Yilmaz, F.L. Meng, W. Lu, J. Abed, C.K.N. Peh, M. Gao, E.H. Sargent, G.W. Ho, Autonomous atmospheric water seeping MOF matrix, *Sci. Adv.* 6 (2020) eabc8605, <https://doi.org/10.1126/sciadv.abc8605>.
- [45] K. Matsumoto, N. Sakikawa, T. Miyata, Thermo-responsive gels that absorb moisture and ooze water, *Nat. Commun.* 9 (2018) 2315, <https://doi.org/10.1038/s41467-018-04810-8>.
- [46] S. Kim, Y. Liang, S. Kang, H. Choi, Solar-assisted smart nanofibrous membranes for atmospheric water harvesting, *Chem. Eng. J.* 425 (2021), 131601, <https://doi.org/10.1016/j.cej.2021.131601>.
- [47] L. Garzón-Tovar, J. Pérez-Carvajal, I. Imaz, D. Maspoch, Composite salt in porous metal-organic frameworks for adsorption heat transformation, *Adv. Funct. Mater.* 27 (2017) 1606424, <https://doi.org/10.1002/adfm.201606424>.
- [48] Y. Sun, A. Spieß, C. Jansen, A. Nuhn, S. Gökpınar, R. Wiedey, S.-J. Ernst, C. Janiak, Tunable LiCl@UiO-66 composites for water sorption-based heat transformation applications, *J. Mater. Chem. A* 8 (2020) 13364–13375, <https://doi.org/10.1039/D0TA03442H>.

- [49] R. Li, Y. Shi, M. Wu, S. Hong, P. Wang, Improving atmospheric water production yield: enabling multiple water harvesting cycles with nano sorbent, *Nano Energy* 67 (2019), 104255, <https://doi.org/10.1016/j.nanoen.2019.104255>.
- [50] Y.L. Hou, Z.Z. Sheng, C. Fu, J. Kong, X.T. Zhang, Hygroscopic holey graphene aerogel fibers enable highly efficient moisture capture, heat allocation and microwave absorption, *Nat. Commun.* 13 (2022) 1227, <https://doi.org/10.1038/s41467-022-28906-4>.
- [51] M.V. Kirov, G.S. Fanourgakis, S.S. Xantheas, Identifying the most stable networks in polyhedral water clusters, *Chem. Phys. Lett.* 461 (2008) 180–188, <https://doi.org/10.1016/j.cplett.2008.04.079>.
- [52] M. Miyazaki, A. Fujii, T. Ebata, N. Mikami, Infrared spectroscopic evidence for protonated water clusters forming nanoscale cages, *Science* 304 (2004) 1134–1137, <https://doi.org/10.1126/science.1096037>.
- [53] X.Y. Zhou, F. Zhao, Y.H. Guo, B. Rosenberger, G.H. Yu, Architecting highly hydratable polymer networks to tune the water state for solar water purification, *Sci. Adv.* 5 (2019), <https://doi.org/10.1126/sciadv.aaw5484> eaaw5484.
- [54] X.P. Li, X.F. Li, H.G. Li, Y. Zhao, J. Wu, S.K. Yan, Z.-Z. Yu, Reshapable MXene/graphene oxide/polyaniline plastic hybrids with patternable surfaces for highly efficient solar-driven water purification, *Adv. Funct. Mater.* 32 (2022) 2110636, <https://doi.org/10.1002/adfm.202110636>.
- [55] M. Okumura, L.I. Yeh, J.D. Myers, Y.T. Lee, Infrared spectra of the solvated hydronium ion: vibrational predissociation spectroscopy of mass-selected $\text{H}_3\text{O}^+(\text{H}_2\text{O})_n(\text{H}_2)_m$, *J. Phys. Chem.* 94 (1990) 3416–3427, <https://doi.org/10.1021/j100372a014>.
- [56] W. Li, X.H. Tian, X.F. Li, S. Han, C.J. Li, X.-Z. Zhai, Y. Kang, Z.-Z. Yu, Ultrahigh solar steam generation rate of a vertically aligned reduced graphene oxide foam realized by dynamic compression, *J. Mater. Chem. A* 9 (2021) 14859–14867, <https://doi.org/10.1039/D1TA03014K>.
- [57] X. Zhou, Y. Guo, F. Zhao, W. Shi, G. Yu, Topology-controlled hydration of polymer network in hydrogels for solar-driven wastewater treatment, *Adv. Mater.* 32 (2020) 2007012, <https://doi.org/10.1002/adma.202007012>.
- [58] W. Li, X.F. Li, W. Chang, J. Wu, P.F. Liu, J.J. Wang, X. Yao, Z.-Z. Yu, Vertically aligned reduced graphene oxide/ $\text{Ti}_3\text{C}_2\text{T}_x$ MXene hybrid hydrogel for highly efficient solar steam generation, *Nano Res.* 13 (2020) 3048–3056, <https://doi.org/10.1007/s12274-020-2970-y>.
- [59] C. Wilson, N.J. Cooper, M.E. Briggs, A.I. Cooper, D.J. Adams, Investigating the breakdown of the nerve agent simulant methyl paraoxon and chemical warfare agents GB and VX using nitrogen containing bases, *Org. Biomol. Chem.* 16 (2018) 9285–9291, <https://doi.org/10.1039/C8OB02475H>.
- [60] I. Kaljurand, A. Kütt, L. Sooväli, T. Rodima, V. Mäemets, I. Leito, I.A. Koppel, Extension of the self-consistent spectrophotometric basicity scale in acetonitrile to a full span of 28 pKa units: unification of different basicity scales, *J. Org. Chem.* 70 (2005) 1019–1028, <https://doi.org/10.1021/jo048252w>.
- [61] V.K. Aggarwal, I. Emme, S.Y. Fulford, Correlation between pKa and reactivity of quinuclidine-based catalysts in the baylis-hillman reaction: discovery of quinuclidine as optimum catalyst leading to substantial enhancement of scope, *J. Org. Chem.* 68 (2003) 692–700, <https://doi.org/10.1021/jo026671s>.
- [62] D.J. Kennedy, B.P. Mayer, S.E. Baker, C.A. Valdez, Kinetics and speciation of paraoxon hydrolysis by zinc(II)-azamacrocyclic catalysts, *Inorg. Chim. Acta* 436 (2015) 123–131, <https://doi.org/10.1016/j.ica.2015.07.035>.
- [63] T. Islamoglu, M.A. Ortuno, E. Prousaloglou, A.J. Howarth, N.A. Vermeulen, A. Atilgan, A.M. Asiri, C.J. Cramer, O.K. Farha, Presence versus proximity: the role of pendant amines in the catalytic hydrolysis of a nerve agent simulant, *Angew. Chem. Int. Ed.* 57 (2018) 1949–1953, <https://doi.org/10.1002/anie.201712645>.
- [64] J.E. Mondloch, M.J. Katz, W.C. Isley III, P. Ghosh, P. Liao, W. Bury, G. Wagner, M. G. Hall, J.B. DeCoste, G.W. Peterson, R.Q. Snurr, C.J. Cramer, J.T. Hupp, O. K. Farha, Destruction of chemical warfare agents using metal-organic frameworks, *Nat. Mater.* 14 (2015) 512–516, <https://doi.org/10.1038/nmat4238>.